International Journal of Plasticity 87 (2016) 15–31

Contents lists available at ScienceDirect

International Journal of Plasticity

journal homepage: www.elsevier.com/locate/ijplas

Discrete dislocation and crystal plasticity analyses of load shedding in polycrystalline titanium alloys

Zebang Zheng [a, *], Daniel S. Balint [b], Fionn P.E. Dunne [a, b]

[a] Department of Materials, Imperial College London, London SW7 2AZ, United Kingdom
[b] Department of Mechanical Engineering, Imperial College London, London SW7 2AZ, United Kingdom

ARTICLE INFO

Article history:
Received 6 June 2016
Received in revised form 25 August 2016
Available online 6 September 2016

Keywords:
A. Dislocations
A. Fracture mechanisms
A. Stress relaxation
B. Crystal plasticity
Cold dwell fatigue

ABSTRACT

The focus of this paper is the mechanistic basis of the load shedding phenomenon that occurs under the dwell fatigue loading scenario. A systematic study was carried out using a discrete dislocation plasticity (DDP) model to investigate the effect of crystallographic orientations, localised dislocation behaviour and grain combinations on the phenomenon. Rate sensitivity in the model arises from a thermal activation process at low strain rates, which is accounted for by associating a stress- and temperature-dependent release time with obstacles; the activation energy was determined by calibrating an equivalent crystal plasticity model to experimental data. First, the application of Stroh's dislocation pile-up model of crack nucleation to facet fracture was quantitatively assessed using the DDP model. Then a polycrystalline model with grains generated using a controlled Poisson Voronoi tessellation was used to investigate the soft-hard-soft rogue grain combination commonly associated with load shedding. Dislocation density and peak stress at the soft/hard grain boundary increased significantly during the stress dwell period, effects that were enhanced by dislocations escaping from pile-ups at obstacles. The residual stress after dwell fatigue loading was also found to be much higher compared to standard fatigue loading. Taylor (uniform strain) and Sachs (uniform stress) type assumptions in a soft-hard grain combination have been assessed with a simple bicrystal DDP model. Basal slip nucleation in the hard grain was found to be initiated by high stresses generated by strong pile ups in the soft grain, and both basal and pyramidal slip nucleation was observed in the hard grain when the grain boundary orientation aligned with that of an active slip system in the soft grain. The findings of this study give new insight into the mechanisms of load shedding and faceting associated with cold dwell fatigue in Ti alloys used in aircraft engines.

1. Introduction

Dwell sensitivity of hexagonal close packed (HCP) α-Ti alloys has been a concern of the aero industry for decades (Adenstedt, 1949; Whittaker, 2011). Representative loading histories of low-cycle fatigue and low-cycle dwell fatigue are shown schematically in Fig. 1. Dwell fatigue is believed to cause the early failure of highly stressed components of gas turbines, such as discs and fan blades (Whittaker, 2011). It has been established that facet fracture, which is the development of a

* Corresponding author.
E-mail address: zebang.zheng12@imperial.ac.uk (Z. Zheng).

http://dx.doi.org/10.1016/j.ijplas.2016.08.009

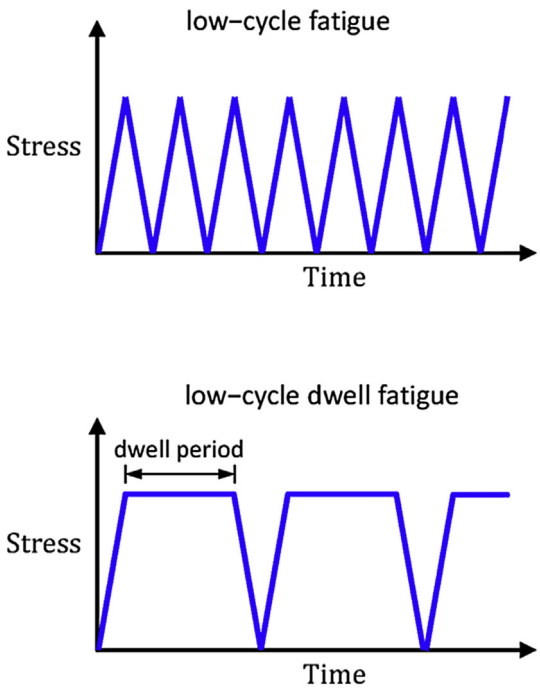

Fig. 1. Schematic illustration of low-cycle fatigue and low-cycle dwell fatigue loading histories.

micro-crack at the grain scale, is often found to be associated with loading that involves a stress-hold (dwell) at room temperature (Sinha et al., 2006). The faceting, particularly when it occurs in a large grain, may lead to a short lifetime, which manifests as dwell sensitivity of the alloy. Early observations, both experimental (Bache et al., 2010; Hasija et al., 2003; Sinha et al., 2006) and analytical (Bache et al., 1997; Bridier et al., 2009; Dunne et al., 2007a, 2007b; Evans and Bache, 1994; Ghosh and Anahid, 2013; Przybyla and McDowell, 2011; Zhang et al., 2015), have shown that the facet crack nucleation process is largely dependent on a particular crystallographic orientation combination: a weakly orientated (soft) grain adjacent to a strongly orientated (hard) grain with respect to the loading direction, referred to as a *rogue* grain combination. However, the mechanistic basis of this important phenomenon is not yet fully understood.

Hasija et al. (2003) reported creep of near-α Ti-6Al alloys under loading. The stress redistribution from the soft grain to the adjacent hard grain, which is known as load shedding, under stress dwell loading was also observed. The simulation results of Dunne and Rugg (2008) and Dunne et al. (2007a) also suggested that the presence of a stress dwell in each loading cycle causes higher damage compared to loading with a strain hold. In 1954, Stroh (1954) established a model to quantify the mode I opening stresses caused by a dislocation pile-up at a grain boundary along possible crack propagation planes in an adjacent grain. This model was further developed and utilised by Bache (1999, 2003) and Evans and Bache (1994) to understand the fatigue performance of titanium alloys. The effects of microstructure and morphology were also discussed systematically by Dunne et al. (2007a, 2007b) and Zhang et al. (2015). However, all of those analyses were conducted at the crystal level, hence cannot provide insight into the dislocation activity within grains or at grain boundaries. If the Stroh method of crack nucleation is indeed occurring in dwell fatigue, then it is important to carefully quantify and understand the dislocation activity near the soft-hard grain boundaries.

Discrete dislocation plasticity (DDP) is a modelling technique in which the motion of individual dislocations is explicitly captured (Van der Giessen and Needleman, 1995). However, classical two-dimensional DDP (Van der Giessen and Needleman, 1995) does not account for thermally activated processes, particularly the escape of dislocations pinned at obstacles via climb or local jog formation, hence classical DDP does not predict rate sensitivity at the low strain rates ($10^{-5}\mathrm{s}^{-1} \leq \dot{\varepsilon} \leq 10^{0}\mathrm{s}^{-1}$) that are associated with the Ti dwell fatigue problem. In this study, we use a mechanistic formalism that incorporates thermally activated dislocation escape (Zheng et al., 2016) into the classical DDP model. A time parameter is assigned to each obstacle that characterises how long it takes a dislocation pinned at that obstacle to overcome the associated energy barrier, hence making a successful escape attempt. The probability of successful attempts is governed by the Gibbs free energy of activation which can be expressed as the summation of the Helmholtz energy and the work done by the external stress field (Gibbs, 1969). The reverse jump from the new equilibrium position is also considered (Dunne et al., 2007a).

In this paper, we aim to provide a systematic analysis of the plastic response of polycrystalline HCP crystals under different loading conditions. A polycrystalline crystal plasticity (CP) model is used to obtain values of the critical resolved shear stress (CRSS) and activation energy associated with dislocation escape from obstacles by calibrating against experimental rate sensitivity results of a Ti-6Al alloy (Hasija et al., 2003). The parameters obtained from the CP calibrations are then used in

corresponding discrete dislocation plasticity simulations to investigate the load shedding phenomenon. A bi-crystal DDP model is used separately to study the effect of grain morphology (i.e. grain boundary orientation relative to the crystal orientations and loading) in the rogue grain combination.

2. Discrete dislocation plasticity and crystal plasticity formulations

The near-α titanium alloy Ti-6Al at room temperature (i.e. $T = 293$ K) is considered in the present study, which was experimentally tested by Hasija et al. (2003) to analyse its creep behaviour and dwell sensitivity. Crystal plasticity and discrete dislocation plasticity models have been developed in an attempt to study the load shedding phenomenon under dwell loading conditions. The formulations of these two models were described in detail in earlier papers (Dunne et al., 2007a, 2007b; Zhang et al., 2015; Zheng et al., 2016), and are concisely summarised here.

2.1. Crystal plasticity framework

The deformation gradient, $\boldsymbol{F}$, can be kinematically decomposed into elastic $\boldsymbol{F}^e$ and plastic $\boldsymbol{F}^p$ tensors as

$$\boldsymbol{F} = \boldsymbol{F}^e\boldsymbol{F}^p \tag{1}$$

The rate of plastic deformation resulting from the crystal slip is

$$\dot{\boldsymbol{F}}^p = \sum_{\alpha} \dot{\gamma}_p^{\alpha}(\boldsymbol{s}^{\alpha} \otimes \boldsymbol{n}^{\alpha}) \tag{2}$$

in which $\boldsymbol{s}^{\alpha}$ and $\boldsymbol{n}^{\alpha}$ are slip direction and plane normal of a given slip system α respectively. $\dot{\gamma}_p^{\alpha}$ is the plastic shear strain rate which is computed according the slip rule. Cottrell and Dexter (1954) related plastic strain rate to the average dislocation glide velocity as

$$\dot{\gamma}_p^{\alpha} = \rho_m v_g b \tag{3}$$

where b is the Burgers vector magnitude, ρ_m the mobile dislocation density and v_g is the average dislocation glide velocity. An expression for the average dislocation glide velocity was developed based on the thermal activation theory first introduced by Gibbs (1969) and utilised by Dunne et al. (2007a), considering both forward and backward escape events from obstacles (each of which requires overcoming the associated energy barrier for escape). Once the resolved shear stress τ^{α} exceeds the critical resolved shear stress τ_c^{α}, plastic flow occurs and the strain rate is given by

$$\dot{\gamma}_p^{\alpha} = \rho_m b^2 \nu_D \exp\left(-\frac{\Delta F}{kT}\right) \sinh\left(\frac{\left(\tau^{\alpha} - \tau_c^{\alpha}\right)\Delta V^{CP}}{kT}\right) \tag{4}$$

where ν_D is the frequency of attempts of dislocations to jump the obstacle escape energy barrier, ΔF the activation energy, k the Boltzmann constant, T the temperature and $\Delta V^{CP} = \gamma_0 b^2/\sqrt{\rho_0}$ is the activation volume, in which γ_0 is a representative shear strain magnitude that is conjugate to the slip system resolved shear stress, and ρ_o is the overall obstacle density.

The critical resolved shear stress of the αth slip system can be calculated based on Taylor's dislocation model (Taylor, 1934) as

$$\tau_c^{\alpha} = \tau_{c0}^{\alpha} + Gb\sqrt{\rho_{SSD} + \rho_{GND}} \tag{5}$$

where τ_{c0}^{α} is the strain-free critical resolved shear stress for given slip system α, G the shear modulus, ρ_{SSD} and ρ_{GND} are the density of statistically stored dislocations (SSDs) and geometrically necessary dislocations (GNDs) respectively. The evolution of SSD density is linearly related to the accumulated slip rate $\dot{p}$ as

$$\dot{\rho}_{SSD} = \gamma' \dot{p} \tag{6}$$

where γ' is the hardening factor.

In this study, a polycrystalline model with grain shapes generated using a controlled Poisson Voronoi tessellation (VGRAIN) (Zhang et al., 2011), as shown in Fig. 2a, was developed for use in the commercial finite-element package ABAQUS; although the CP model is 3D, the grain shapes are invariant in the z-direction and the model was subjected to plane strain constraint with respect to the z-direction. An average 15 μm^2, minimum 10 μm^2, and maximum 20 μm^2 grain size have been specified with a regularity parameter of 0.9. A rogue grain combination is located in the central region and surrounded by other randomly orientated soft grains. The σ_{yy} stress along the $A - A'$ path, as indicated in Fig. 2c, was recorded through the loading history.

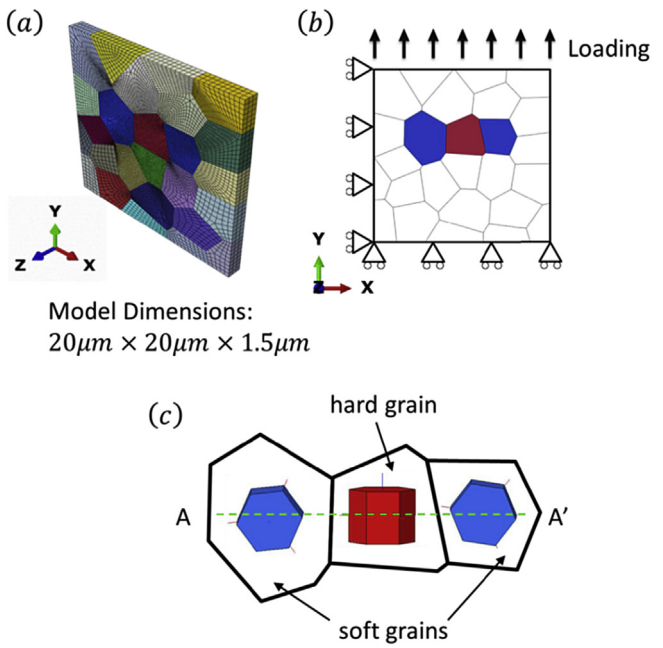

Fig. 2. Polycrystalline Ti-6Al model: (a) 3D crystal plasticity model subjected to a plane strain constraint; (b) 2D plane strain discrete dislocation plasticity model; (c) crystal orientations in a rogue grain combination with the location of the A–A′ path shown.

2.2. Discrete dislocation plasticity formulation

A small-strain, two-dimensional, plane strain discrete dislocation formulation was used to simulate the polycrystal shown in Fig. 2b. The grain shapes and crystallographic orientations of each grain are identical to those in the crystal plasticity model for the sake of the comparison study. There are three $\langle a \rangle$-prismatic slip systems in the soft grains as shown in Fig. 3a. The orientations of the soft grains can be chosen arbitrarily, in terms of rotations of the slip systems depicted in Fig. 3a about the z-axis. The slip systems in the hard grain consist of one $\langle a \rangle$-basal slip system together with two 1st order $\langle c + a \rangle$ pyramidal slip systems, as shown in Fig. 3b; again, any rotation about the z-axis is possible. The sets of slip systems shown in Fig. 3 satisfy the plane strain constraint of the 2D problem.

The polycrystal is subjected to uniaxial loading along the y-direction, and the bottom and left faces are constrained as shown in Fig. 2b. In addition, the back surface is fixed in the z-direction in the crystal plasticity model to prevent translation in that direction. The right face (and front in the CP model) is traction free and dislocations are permitted to escape from these surfaces in the DDP model. The boundary conditions are achieved in the DDP model using the linear superposition method introduced by Van der Giessen and Needleman (1995). The model consists of 150 × 150 finite elements and is refined around the rogue grain combination in order to obtain convergent results.

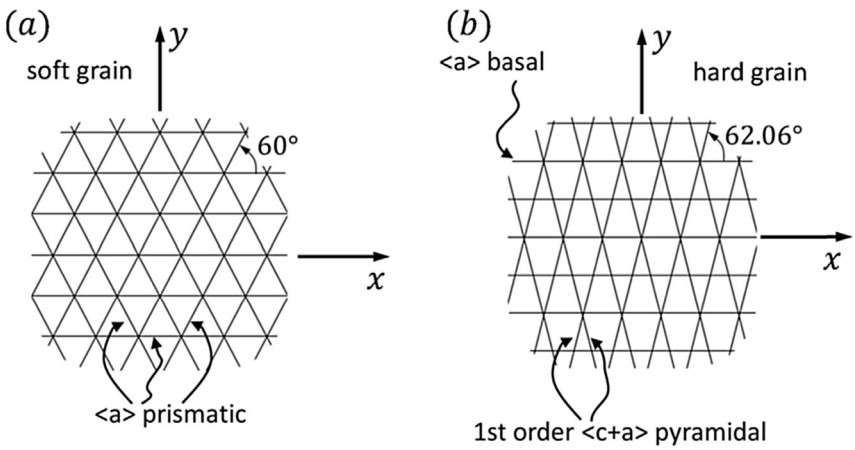

Fig. 3. Schematic diagrams of slip systems in the (a) soft and (b) hard grains.

The model is initially dislocation free with slip planes spaced 100b apart. Frank-Read sources and obstacles are randomly distributed on all slip planes with densities ρ_{nuc} and ρ_{obs}. A dislocation dipole is nucleated from a source once the resolved shear stress τ exceeds the source strength τ_{nuc} for a period of time t_{nuc}. The source strengths are chosen from a normal distribution with mean value $\overline{\tau}_{nuc}$ and standard deviation $0.2\overline{\tau}_{nuc}$. The nucleation time is estimated by Agnihotri and Van der Giessen (2015) as

$$t_{nuc} = \eta_1\eta_2\frac{\phi}{\tau b} \tag{7}$$

in which 2ϕ is the source length, η_2 is a constant related to the viscous drag coefficient B and η_1 is an enhancement factor. The initial dipole spacing is chosen such that the attraction stress between dislocations is equilibrated by the applied resolved shear stress τ_{nuc}, which gives

$$L_{nuc} = \frac{Gb}{2\pi\,\tau_{nuc}(1-\nu)} \tag{8}$$

where G and ν are the shear modulus and Poisson's ratio. Once the dislocations are nucleated from the sources, they are free to glide along the slip plane until they meet an obstacle or other dislocations, and the velocity is given by the mobility law as

$$v = \frac{\tau b}{B} \tag{9}$$

where B quantifies the drag. When two dislocations on the same plane with opposite Burgers vector are within the critical annihilation distance $L_e = 6b$, they are removed. Further details of a typical plane strain DDP formulation can be found in the literature, e.g. (Balint et al., 2006, 2008; Tarleton et al., 2015; Van der Giessen and Needleman, 1995).

Each obstacle is assigned a thermal activation-related, stress-associated time parameter t_{obs}, which is the residency time of a dislocation at the obstacle before it escapes. The time can be calculated as the inverse of the successful jump frequency, i.e. $t_{obs} = 1/\Gamma$. The frequency of successful jumps is governed by a rule that is similar to that used in the crystal plasticity model described in Zheng et al. (2016)

$$\Gamma = \frac{\nu_D b}{l_{obs}}\exp\left(-\frac{\Delta F}{kT}\right)\sinh\left(\frac{\tau\Delta V^{DD}}{kT}\right) \tag{10}$$

in which l_{obs} is the average obstacle spacing, ΔF is the activation energy, ν_D is the frequency of attempts of dislocations to jump the energy barrier and ΔV^{DD} is the activation volume. It is worth pointing out that in Eq. (10), the shear stress τ appears rather than $\tau-\tau_c$ as in Eq. (4). In the crystal plasticity model, plastic slip only occurs when the critical resolved shear stress is exceeded. In DDP, slip arises directly from the dislocations in the system, hence if dislocations exist (i.e. they have already been nucleated) they will move according to Eq. (9) without needing to exceed a threshold stress.[1] In the same way, when a dislocation is pinned at an obstacle it does not need to exceed a threshold value for the thermal activation event to begin, even if the stress is lower than the source strength, although residency is prolonged at lower stress. The friction stress for glide is usually neglected, especially at the low strain rate regimes. As discussed in Zheng et al. (2016), the time constant associated with free flight is much shorter compared to that for the thermally activated obstacle escape process. Even if Eq. (9) was developed to include the Peierls barrier, the time elapsed for dislocations travelling between obstacles is negligible.

We note that there are two independent parameters controlling the thermal-activation based slip rate equation: activation volume ΔV and the activation energy ΔF. The activation volume utilised in the crystal plasticity model is determined by Zhang et al. (2015) for Ti-6Al as $\Delta V^{CP} = 18.75b^3$ which is within the appropriate range for α-Ti alloys ($8b^3$–$80b^3$) given by Conrad (1967). The methodology adopted considered a polycrystalline model of 7.5 μm × 2.5 μm (thickness 1.5 μm for the crystal plasticity model) which was used to calibrate against the experimental data of Hasija et al. (2003). The crystallographic orientations were chosen to be randomly rotated soft grains as defined in Fig. 3a. The CRSS and activation energy were chosen so that the stress-stain responses give the correct rate sensitivity. The other parameters used in the CP model are chosen to represent Ti-6Al at room temperature (Zhang et al., 2015). The value of ΔF and the other CP parameters given in Table 1 give good agreement between the CP and experimental results, as shown in Fig. 4a.

The slip rate representations for crystal and discrete dislocation plasticity controlled by Eqs. (4) and (10) respectively differ because slip system back stress has to be included explicitly within the CP formulation while in the DDP model, the slip system back stress developed from dislocation accumulation and pile-up is accounted for naturally. Hence the slip driving stresses τ^* are given by $\tau^* = \tau^\alpha - \tau_c^\alpha$ and $\tau^* = \tau$ in the CP and DDP models respectively. A consequence is that the activation volumes needed for the two models are different to ensure the same work done $\tau^*\cdot\Delta V$ for slip is achieved. The optimal DDP activation volume ΔV^{DD} to capture the same rate sensitive response is found to be $0.5b^3$. Using the properties given in Table 1,

[1] Unless a friction stress is included in the mobility law, which is not used here.

Table 1
Model properties used unless stated otherwise.

General properties:						
G (MPa)	ν	b (nm)	ΔF (J/atom)	ν_D (Hz)	k (JK^{-1})	
39500	0.33	0.32	9.913×10^{-20}	10^{11}	1.38×10^{-23}	
Crystal plasticity properties:						
$\rho_0(\mu m^{-2})$	$\rho_m(\mu m^{-2})$	γ_0	$\tau_{c0}^{\langle a\rangle}(MPa)$	$\tau_{c0}^{\langle c+a\rangle}(MPa)$	γ'	
0.01	5.0	6×10^{-4}	280	840	0.05	
Discrete dislocation plasticity properties:						
B (Pa·s)	ΔV^{DD}	$\overline{\tau}_{nuc}^{\langle a\rangle}$(MPa)	$\overline{\tau}_{nuc}^{\langle c+a\rangle}$(MPa)	η_1	η_2	$\rho_{nuc}(\mu m^{-2})$	$\rho_{obs}(\mu m^{-2})$
10^{-4}	$0.5b^3$	440	1320	10	9B	5	20

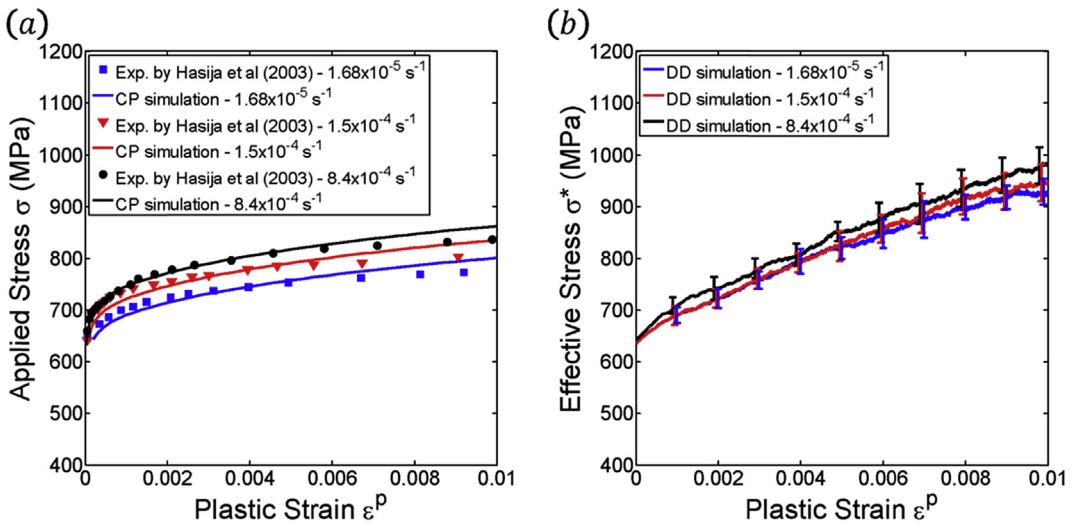

Fig. 4. Strain rate sensitivity calibration with polycrystalline Ti-6Al alloy.

and considering fifty pinned dislocations undergoing potential escape by thermal activation, the DDP calculation for uniaxial tension gives the work done on these dislocations to be between 1.44~4.32 $\times 10^{-20}$ J. At the corresponding location within the CP model, the work done is found to be between 2.46~3.69 $\times 10^{-20}$ J. Although the work done range is slightly broader for the DDP model, due to differing numbers of dislocations in each pile-up group, the slip energies for each model are seen to be very close. The mean and standard deviation of the source strength in the DDP model were chosen so that the flow stress of a single crystal under displacement controlled loading is consistent with that of the CP model.

All the required properties for the DDP model are summarised in Table 1, and the resulting uniaxial stress-strain response for differing applied strain rates is shown in Fig. 4b. The DDP predicted hardening is stronger, as shown in Fig. 4b, but the flow stress spacing under the three different strain rates is well captured; the former is due to the impenetrable grain boundaries assumption in the DDP model, hence could be improved using an appropriate slip transmission rule that is more representative of grain boundaries. The DDP curves shown in Fig. 4b are averages of ten independent analyses to reduce the stochastic nature of discrete dislocation plasticity. The full set of CP and DDP modelling parameters are listed in Table 1.

3. Stroh's model

In 1954, Stroh established a model for crack nucleation by considering the equilibrium state of a dislocation pile-up in an infinite elastic medium under applied shear stress τ_0 (Stroh, 1954). The formulation provides a quantitative expression for the normal, or mode I opening stress on an inclined plane in one grain due to a dislocation pile-up in an adjacent grain. The original derivation by Stroh considered a remotely applied pure shear stress τ_0 parallel to the pile-up plane, as depicted in Fig. 5a, such that the resolved shear stress on the pile-up is the same as the applied stress (crucially, the applied stress also contributes to the crack opening stress σ_n). The boundary conditions considered in some subsequent works e.g (Bache, 2003; Evans and Bache, 1994) are different to those relevant to Stroh's equation for σ_n. As such, Stroh's original model cannot be used directly for remote loadings other than pure shear parallel to the pile-up plane, but Stroh's equation for σ_n can be rederived without much difficulty for other applied loadings. The derivation of the crack opening stress σ_n under both pure shear and uniaxial tension conditions are discussed in this section and corresponding discrete dislocation models have been built to validate the resulting expressions.

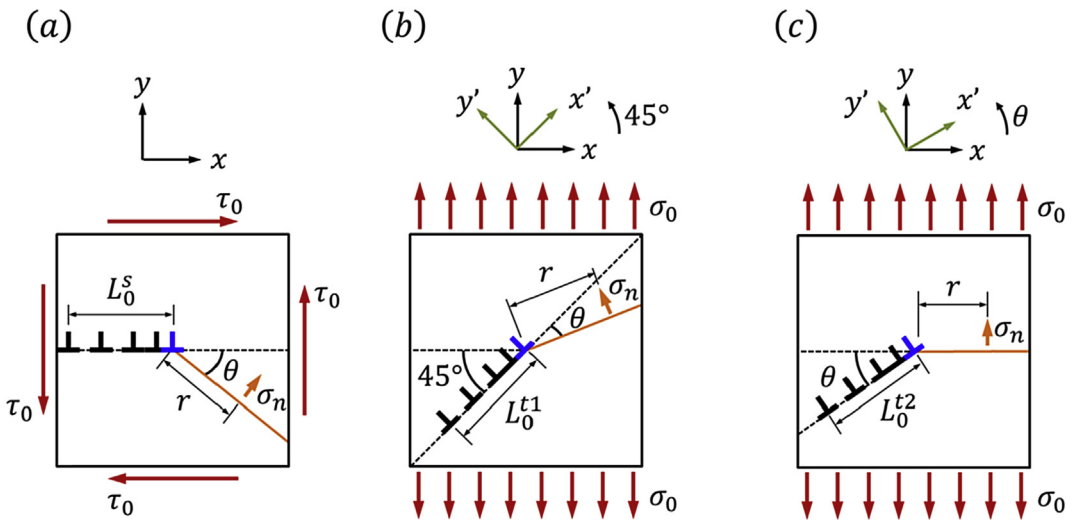

Fig. 5. Schematic diagram of Stroh's model. (a) The original pure shear model; (b) the new uniaxial tension model I; (c) the new uniaxial tension model II.

3.1. Pure shear model

The original model considered N positive edge dislocations piled up along the x-axis in response to an applied pure shear parallel to the pile-up plane, τ_0, with the lead dislocation pinned at the origin, as shown in Fig. 5a. The $(N-1)$ dislocations behind the pinned lead dislocation are free to move in the slip plane, and their equilibrium positions can be obtained from the zeros of the derivative of the Nth Laguerre polynomial. The length of the pile up group is given by Stroh (1954)

$$L_0^s = \frac{GbN}{\pi(1-\nu)\tau_0} \tag{11}$$

where G is the shear modulus, b the Burgers vector and ν is Poisson's ratio. The normal stress σ_n on the plane oriented by θ with respect to the positive x-axis (measured positively as indicated) is given as a function of the direction angle, θ, and the distance from the front of the pile-up, r. The stress normalised by the applied shear stress is (Stroh, 1954)

$$\frac{\sigma_n}{\tau_0} = \frac{3}{2}\left(\frac{L_0^s}{r}\right)^{\frac{1}{2}} \sin\theta \cos\frac{1}{2}\theta \tag{12}$$

By differentiating Eq. (12), it is possible to determine that when $\theta = 70.5°$, the normal stress is maximal. A discrete dislocation model has been built to corroborate Stroh's model. The dimension of the model is 10 μm × 10 μm and pure shear is imposed on the model by prescribing a periodic boundary condition as described by Balint et al. (2008).

$$\Delta u_i = \bar{\varepsilon}_{ij}\Delta x_j \tag{13}$$

in which Δu_i is the displacement difference between opposite sides of the model defined by the relative position vector Δx_j, and $\bar{\varepsilon}_{ij}$ is the applied strain tensor, specified as $\bar{\varepsilon}_{12} = \bar{\varepsilon}_{21} = \gamma/2$ and $\bar{\varepsilon}_{11} = \bar{\varepsilon}_{22} = 0$ for pure shear. To test the Stroh model, 100 positive edge dislocations were distributed on the negative x-axis with an even spacing and the lead dislocation was pinned at the origin. The finite element mesh used to solve the boundary conditions correction problem (Van der Giessen and Needleman, 1995) was highly refined around the pile-up zone in order to accurately resolve the stresses there: 10^4 quadratic finite elements were used in a 0.5 μm × 0.5 μm region. An adaptive time step was used to obtain the equilibrium positions of the dislocations. The normal stress σ_n versus the distance from the front of the pile-up r at different angles θ is shown in Fig. 6. There is good agreement between the DDP simulations and Stroh's analytical solution, although very near the lead dislocation in the DDP model ($r < 0.005$ μ m) a small discrepancy arises as a result of persistent small oscillations in the 2nd dislocation's position that are felt at that location, which cannot be completely eliminated even at very small time steps; the trends are unaffected by this. The normal stress was found to be inversely proportional to $\sqrt{r}$ at fixed angle as shown in Fig. 6a for one value of θ, that which maximises σ_n. For a fixed value of r, the normal stress varies with θ, and the variation with θ is more pronounced at a location closer to the tip. The normal stress is maximal when $\theta = 70.5°$, consistent with the Stroh solution.

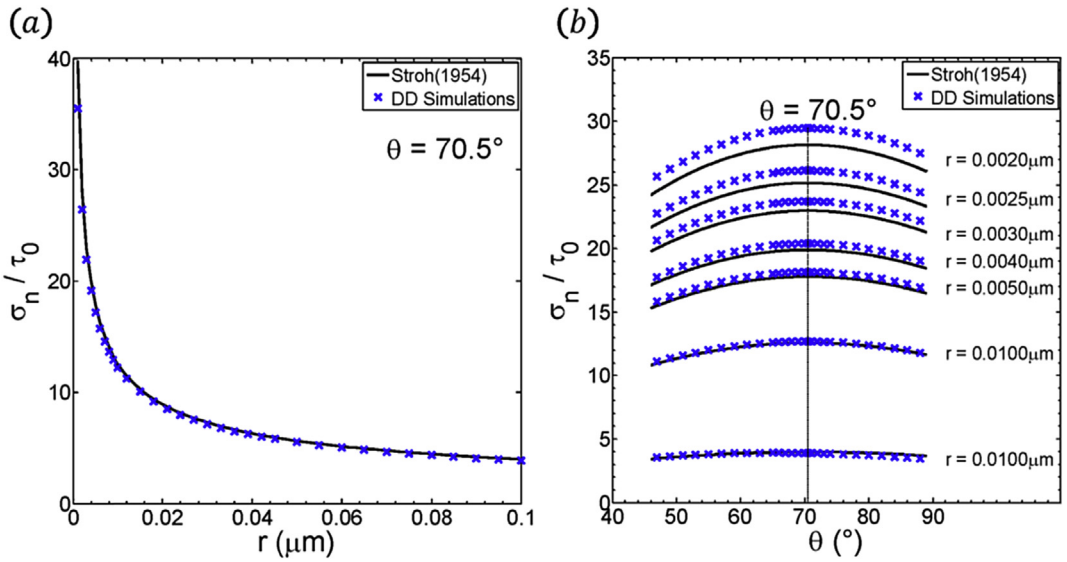

Fig. 6. Comparison of discrete dislocation predictions with the analytical solution of the pure shear model. (a) Normalised normal stress versus distance from the pile up group at fixed angle 70.5°; (b) normalised normal stress versus angle at fixed distance.

3.2. Uniaxial tension model

Stroh's model adapted for remotely applied uniaxial tension σ_0 is illustrated in Fig. 5b and c for two different configurations. In order to directly compare uniaxial tension to pure shear, model I (Fig. 5b) is used; the pile-up plane is oriented 45° with respect to the positive x-axis in order to maximise the resolved shear stress from the applied loading σ_0 and the crack plane is oriented by an angle θ with respect to the pile-up plane, as in the original Stroh model. The length of the pile up group is given by (see Appendix A for details)

$$L_0^{t1} = \frac{GbN}{2\pi(1-\nu)\sigma_0} \tag{14}$$

The corresponding normalised normal stress is given by (see Appendix A for details)

$$\frac{\sigma_n}{\sigma_0} = \frac{3}{4}\left(\frac{L_0^t}{r}\right)^{\frac{1}{2}} \sin\theta\cos\frac{1}{2}\theta + \frac{1}{2} \tag{15}$$

By differentiating Eq. (15), it is found that when $\theta = 70.5°$, the normal stress is maximal, which is the same as the original pure shear model.

Uniaxial tension model II shown in Fig. 5c is also considered, as this configuration is that which is relevant to facet fatigue, since in that case the orientation of the pile-up plane in the soft grain is variable and fracture is known to occur on a basal plane perpendicular to the loading in the adjacent hard grain. In this model, the pile-up plane is oriented by an angle θ with respect to the positive x-axis and the crack plane is fixed in the horizontal position. The normal stress is calculated at the point (r,0) located on the positive x-axis. The length of the pile up group is given by (see Appendix B for details)

$$L_0^{t2} = \frac{GbN}{\pi(1-\nu)\sigma_0\cos\theta\sin\theta} \tag{16}$$

where σ_0 is the applied stress. It is worth noting that unlike the pure shear and uniaxial tension I models, the pile-up length is a function of the slip direction θ. The corresponding normalised normal stress is given by (see Appendix B for details)

$$\frac{\sigma_n}{\sigma_0} = \frac{3}{2}\left(\frac{L_0^{t2}}{r}\right)^{\frac{1}{2}} \sin^2\theta\cos\theta\cos\frac{1}{2}\theta + \frac{1}{2}\sin^2 2\theta \tag{17}$$

The solution is more complex than the pure shear model. The angle that gives the maximum normal stress on the crack plane is a function of the distance from the pile-up tip; it was invariant with distance in the other two models. In the limit

$r \to 0$, a pile-up plane oriented 56.1° from horizontal gives the greatest crack opening stress; this is easily achieved by the soft grain orientation depicted in Fig. 2, which has three independent $\langle a \rangle$ prism planes separated by 60° from each other. In this model the pile-up group represents the slip within a favourably orientated grain, i.e. soft grain, terminating at the grain boundary. The length of the pile-up L_0^{t2} can be estimated as the half length of the soft grain. The normal stress in the adjacent 'hard' grain is interpreted as that responsible for fatigue crack nucleation, and as in the other models, depends not only on the remote applied loading but also on the local stress state caused by the pile-up. Although these models provide a simple interpretation of crack nucleation, they do not account for the time dependence of the loading, i.e. the effect of the stress dwell, nor the effect of grain boundary morphology. These effects are addressed in the next section using a polycrystalline DDP model.

4. Load shedding in Ti-6Al polycrystal response

Load shedding has been identified as the fundamental mechanism in the development of facet cracks (Sinha et al., 2006; Venkataramani et al., 2008; Venkatramani et al., 2007). The load shedding phenomenon is always associated with a rogue grain combination under stress dwell fatigue loading at ambient temperature (Dunne et al., 2007b; Hasija et al., 2003; Venkataramani et al., 2008; Venkatramani et al., 2007). The stress in the soft grain redistributes to the adjacent hard grain during the stress-hold period as a result of creep. A comparison study has been carried out to understand the phenomenon, especially the role of the dislocation structure at the soft-hard grain boundary. Two types of loading are considered (see inset Fig. 7): normal fatigue loading and dwell fatigue loading. The increase and decrease to and from the peak stress occur in 12s at a constant rate, and the dwell period is 4s. Although the dwell is much shorter than is usually considered appropriate, it is long enough to show clear evidence of load shedding while making the simulations feasible in terms of computing time. The magnitude of the peak applied stress (sustained during the dwell) is 711 MPa to ensure plasticity occurs in the soft grains (Zhang et al., 2015).

Contours of the normal stress relevant to facet crack opening (σ_{yy}) in the rogue grain combination (the surrounding grains are omitted for clarity) are plotted in Fig. 7 for different stages in the loading, together with the associated dislocation structures. By comparing Fig. 7(a) and (b) it is apparent that the stress at the soft-hard grain boundaries increased significantly as a result of the dwell at peak stress. There is more dislocation activity in the soft grains, which enhances dislocation pile-ups at the grain boundaries relative to a cycle without a dwell. Fig. 7(c) and (d) show the stress at the end of unloading under normal fatigue and dwell fatigue loading, respectively. The stress in the hard grain is again highly localised in the grain boundary regions in the dwell fatigue case, but is much more diffuse when there is no dwell. It is worth noting that there are a few basal dislocations nucleated in the hard grain under the dwell scenario, particularly after unloading, which does not happen under normal fatigue loading (no dwell).

Figs. 8 and 9 compare the σ_{yy} stress along the A – A′ path (see Fig. 2) using crystal plasticity (CP) (Figs. 8a and 9a) and discrete dislocation plasticity (Figs. 8b and 9b). The stress along the A – A′ path in the DDP calculation is the average of 20 parallel paths spaced by 0.05 μm centred about the hard grain centreline through the rogue grain combination to distinguish

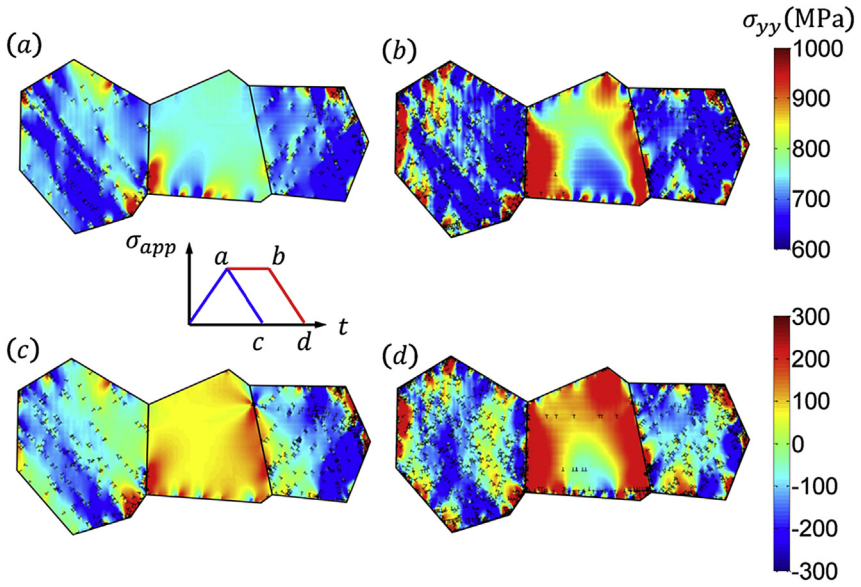

Fig. 7. σ_{yy} stress contours with the dislocation structure superimposed at (a) the end of the rise in applied stress to its peak value; (b) the end of the dwell; (c) the end of unloading under normal fatigue loading and (d) the end of unloading under dwell fatigue loading.

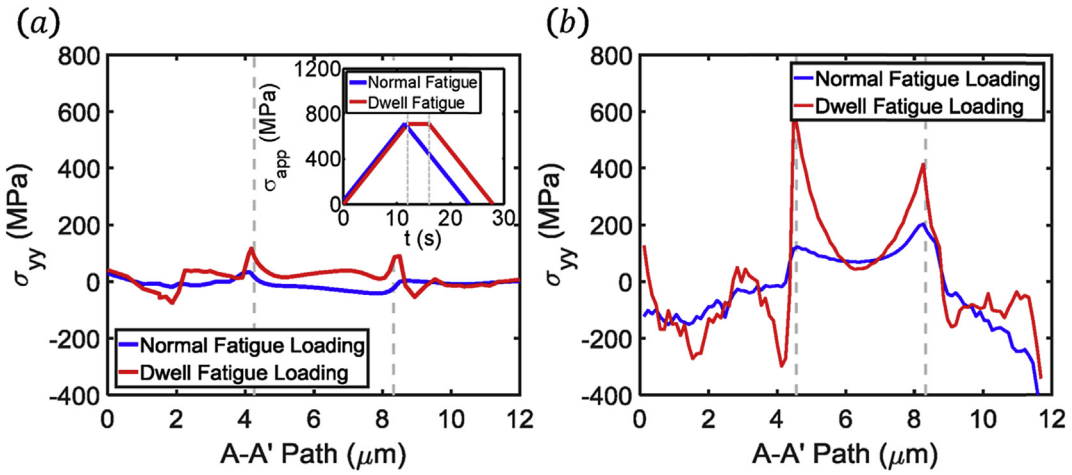

Fig. 8. σ_{yy} stress along the A–A′ path at the end of normal fatigue and dwell fatigue loading after complete unloading using (a) crystal plasticity and (b) discrete dislocation plasticity.

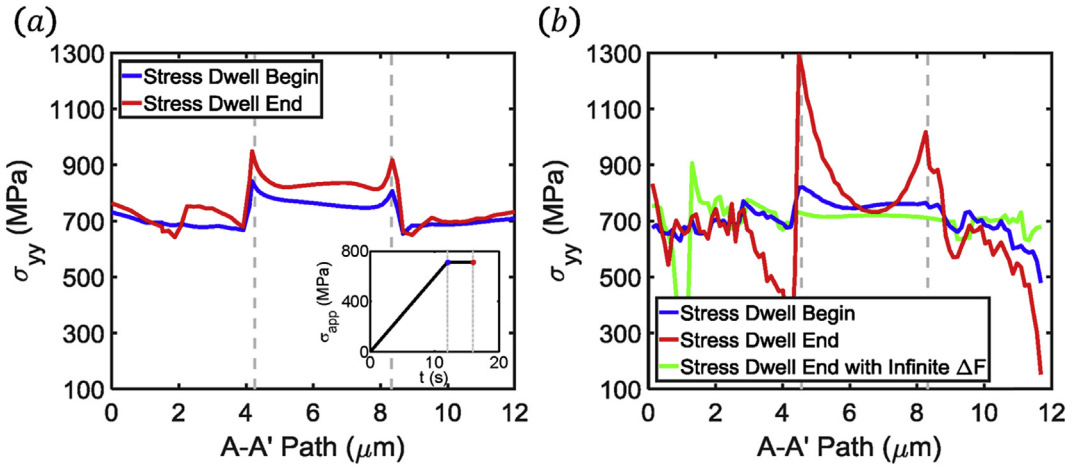

Fig. 9. Comparison of σ_{yy} stress along the A–A′ path before and after the dwell at peak stress using (a) crystal plasticity and (b) discrete dislocation plasticity.

the trend from the statistical variations. The residual stresses after complete unloading under normal fatigue and dwell fatigue loading are plotted in Fig. 8. In both models, a higher residual stress is predicted at the grain boundaries in the dwell scenario, but the effect is much more pronounced using DDP compared to CP. The redistribution of stress from the soft grain to the hard grain in the grain boundary region, known as load shedding, occurs primarily during the dwell, as shown in Fig. 9. While stress is held at its peak value, dislocations continue to nucleate in the soft grains and pile up at the soft-hard grain boundaries, an effect not captured by the CP model due to the averaged description of plastic flow in CP compared to DDP, which accounts for all dislocations individually; the influence of thermally activated dislocation escape from obstacles is very important here, as shown in Fig. 9b by the dwell case with very high activation energy to prevent escape, since this relieves the back stresses on sources caused by pile-ups, allowing them to continue nucleating. By the continued activation of sources in the soft grains during the dwell, the stress in the soft grain is relaxed, and correspondingly increased in the hard grain (which deforms nearly elastically due to the relative absence of dislocations) via the enhancement of dislocation pile ups in the soft grains at the soft-hard grain boundaries.

The dislocation density evolution of the left soft grain is plotted in Fig. 10. The dislocation density increased by a factor of four over the course of the dwell period relative to the normal fatigue condition, although it decreased somewhat during the unloading. The resultant dislocation density in the soft grain at the end of one dwell fatigue loading cycle is 77.38 μm^{-2} which is consistent with the experimental measurement of dislocation density (10^2~10^3 μm^{-2}) in Ti-6Al-4V after small-strain deformation (Littlewood et al., 2011). The importance of thermally activated dislocation escape from obstacles is also evident in the much lower dislocation density observed when the activation energy is very high to prevent escape, as shown in Fig. 10; again, this is because thermally activated escape allows sources to continue nucleating, thereby generating more dislocations. It is

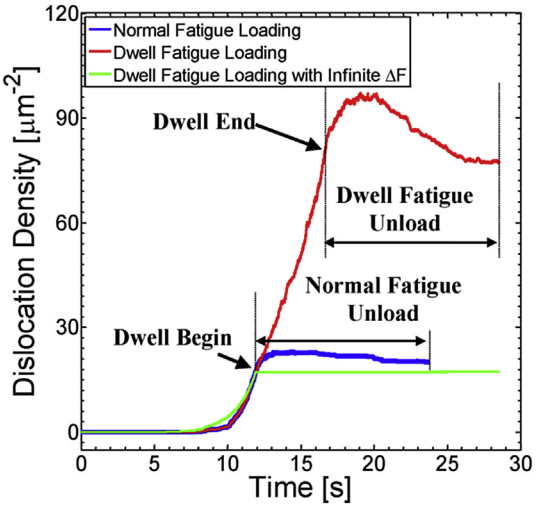

Fig. 10. Dislocation density evolution of the left soft grain.

noted that the dislocation density is still increasing through roughly the first third of the unloading period in the dwell case. This is due in part to a short dwell period that prevents the soft grain from reaching an equilibrium dislocation structure. In the case where thermally activated escape is prevented, sources are not activated because the back stresses from pile-ups make further activation under the influence of the constant applied stress impossible; as a result the dislocation density remains constant during the dwell period. When thermally activated escape is allowed to occur in the dwell case, the time to achieve an equilibrium dislocation structure is longer since the structure is allowed to adjust further by escape over time, which is evident in Fig. 10. In either case, once unloading begins dislocation annihilation increases primarily by reverse glide, while nucleation decreases and eventually ceases, causing the dislocation density to decrease until a stable value is reached.

5. Grain boundary morphology effect

The grain shapes used to analyse the load shedding phenomenon were generated by a controlled Poisson Voronoi tessellation to represent the morphology of the polycrystal in a statistically equivalent way in terms of the grain size and grain orientation distributions. It has been reported in Dunne et al. (2007b) that the relationships between the grain orientations, the grain boundary morphology and the loading direction influences dwell fatigue. A bicrystal DDP model, 2 μm × 2 μm, was used to study the effect of grain boundary orientation relative to the soft-hard grain combination and the loading direction on load shedding. The soft and hard grains were initially the same dimensions and were assigned the crystallographic orientations depicted in Fig. 11a. The orientation of the grain boundary, however, was characterised by the angle θ with respect to the positive x-axis. The bicrystal was subjected to uniaxial tension in the y-direction and both displacement and stress controlled loading were considered.

Fig. 12 shows the results of displacement controlled loading. The bicrystal was stretched to 1% strain at a constant strain rate $\dot{\varepsilon} = 8.4 \times 10^{-4}\text{s}^{-1}$ in approximately 12s. The slip distributions for two selected grain boundary orientations are presented. The slip was quantified in the usual way as the sum of the absolute values of the resolved shear strains on the three slip systems, i.e. $\omega = \sum_{m=1}^{3}|\gamma^m|$, where γ^m is the resolved shear strain on slip system m given by $\gamma^m = s_i^m \varepsilon_{ij} n_i^m$, where $\boldsymbol{s}^m$ is the slip direction and $\boldsymbol{n}^m$ is the slip plane normal (Balint et al., 2006). When the grain boundary is such that θ<45°, the grains are in series with respect to the loading direction, generating a Sachs condition (the stresses in each grain are the same). This allows the applied strain to be accommodated predominately by the soft grain deforming plastically, and as a result the hard

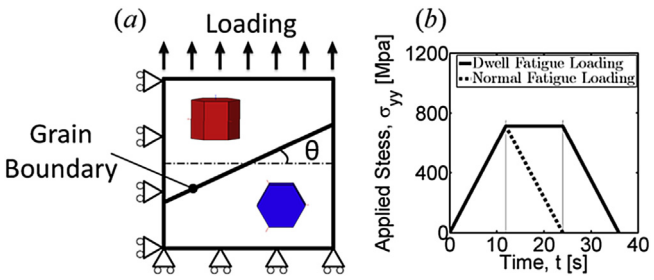

Fig. 11. (a) Bicrystal model of rogue grain combination with boundary conditions; (b) stress controlled loading.

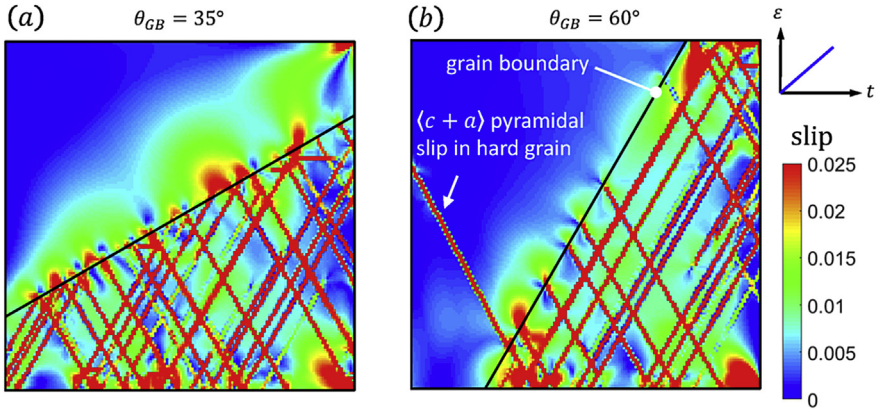

Fig. 12. Slip distribution under displacement controlled loading for a grain boundary angle of (a) $\theta_{GB} = 30^\circ$ and (b) $\theta_{GB} = 60^\circ$.

grain remains elastic. On the other hand, when θ>45°, e.g. 60°, the grains are in parallel and the hard and soft grains are subjected to the same amount of uniaxial strain, thus generating a Taylor condition. When the soft grain reaches its yield stress, ⟨a⟩ prismatic slip occurs and the rate of increase in the overall applied stress required to achieve the applied strain decreases, however the resolved shear stresses on the slip systems in the hard grain keep increasing because those systems are stronger (higher source strength). When the stress is high enough, the weakest ⟨$c + a$⟩ pyramidal source in the hard grain is activated and ⟨$c + a$⟩ pyramidal slip is generated as shown in Fig. 12b. Note that in the latter (Taylor) example, the grain boundary orientation $\theta_{GB} = 60^\circ$ is parallel to the active prismatic slip system in the neighbouring soft grain.

To examine stress controlled loading, both normal fatigue loading and dwell fatigue loading (as shown in Fig. 11b with maximum stress 711 MPa) were imposed on the bicrystal with a fixed grain boundary angle $\theta = 60^\circ$, such that the grain boundary orientation is parallel to the active prismatic slip system in the soft grain. This combination under strain-controlled loading led to the initiation of ⟨$c + a$⟩ pyramidal slip in the hard grain and was referred to as a crystallographic–morphological interaction by Dunne et al., 2007b in their crystal plasticity analysis. The slip contours at different stages in the loading are shown in Fig. 13. At the end of the increase in stress (Fig. 13a), multiple ⟨a⟩ prismatic slip lines are

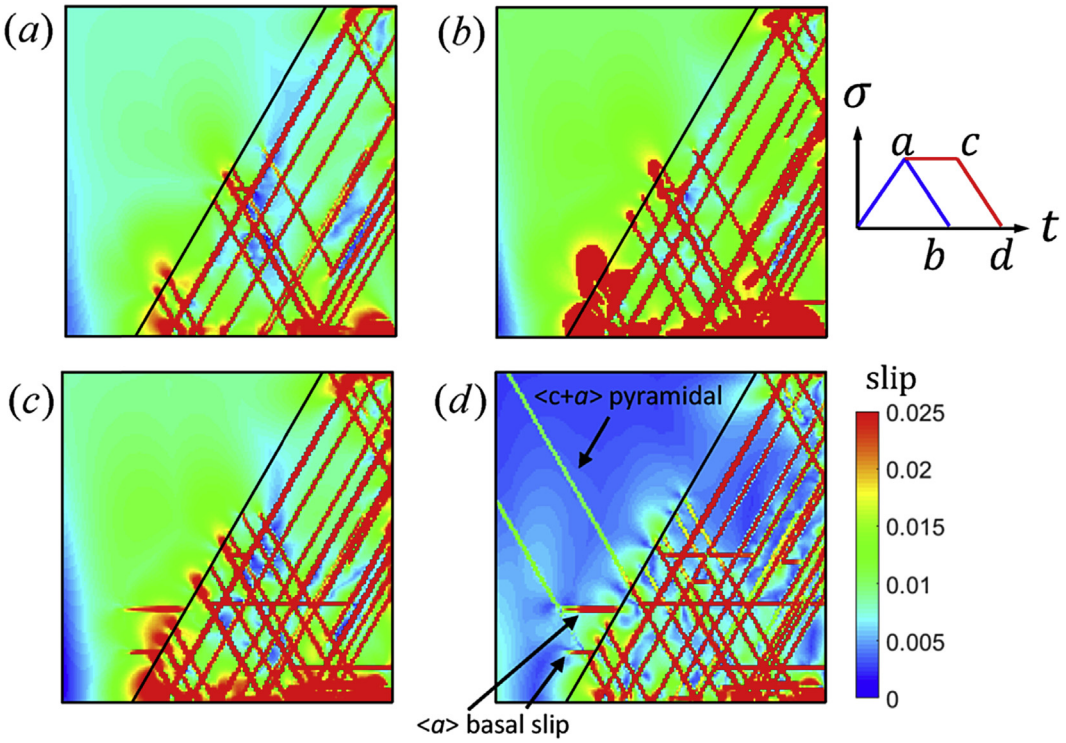

Fig. 13. Slip distribution under stress control for a grain boundary angle of $\theta_{GB} = 60^\circ$. (a) End of the loading period; (b) end of the unloading under normal fatigue; (c) end of the dwell; (d) end of the unloading under dwell fatigue.

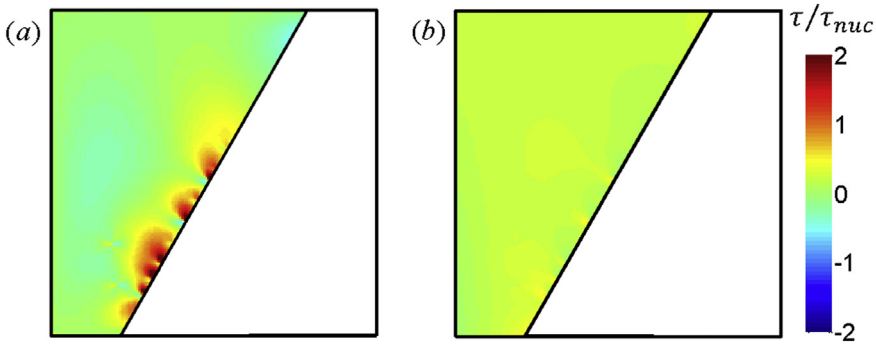

Fig. 14. Normalised resolved shear stress on one of the $\langle \mathbf{c}+\mathbf{a} \rangle$ pyramidal slip systems in the hard grain at the end of (a) dwell fatigue loading and (b) normal fatigue loading.

apparent in the soft grain while no slip has occurred in the hard grain. After normal fatigue unloading, the slip distribution does not change significantly. On the contrary, at the end of the dwell period more $\langle a \rangle$ prismatic slip lines are apparent in the soft grain, together with two $\langle a \rangle$ basal slip planes activated in the hard grain near the grain boundary as a result of dislocation pile-ups in the soft grain at the soft-hard grain boundary (the resolved shear stress on the basal plane from the applied loading is zero). At the end of unloading in the dwell scenario, the localised but highly active $\langle a \rangle$ basal slip planes remain and two long ranging weak $\langle c+a \rangle$ pyramidal slip planes are developed. The $\langle a \rangle$ basal activation is largely statistical since it requires the close proximity of a suitable pile-up in the soft grain, in order to establish the resolved shear stress necessary to nucleate basal slip in the hard grain. Several 0° $\langle a \rangle$ prismatic planes are also active in the soft grain under the stress controlled loading, although this too is largely statistical since it is instigated by other dislocations, not the applied loading. Contours of the resolved shear stress τ at the end of the unloading on one of the $\langle c+a \rangle$ pyramidal slip systems in the hard grain are plotted in Fig. 14 for the normal fatigue and dwell fatigue scenarios. The stress is normalised by the mean value of the pyramidal source strength, i.e. $|\tau/\tau_{nuc}|>1$ indicates that the stress is, on average, high enough to activate plasticity. The stress under normal fatigue loading is homogeneous and less than $0.5\tau_{nuc}$ because the dislocation density is lower and a greater proportion of the dislocations in the soft grain remain in the core of the grain, i.e. pile ups are lower in intensity. However, under dwell fatigue loading, more dislocations are generated in the soft grain resulting in higher intensity pile ups at the soft-hard grain boundary, which increases the stress in the grain boundary region in the hard grain; it is the local stress, rather than the applied stress, generated by these pile up dislocations in the soft grain that activate slip in the hard grain, particularly on the $\langle a \rangle$ basal system since the resolved shear stress on that system caused by the applied loading is zero.

6. Conclusion

2D discrete dislocation plasticity calculations have been carried out to analyse the load shedding associated with dwell fatigue in polycrystalline Ti alloys for the first time. The DDP formulation includes thermally activated dislocation escape from obstacles, which is the source of the strain rate sensitivity in the model. Material parameters were determined by calibrating a companion crystal plasticity model to experimental data. The DDP model was first used to validate and explore the idea proposed by Stroh (1954), that crack nucleation could be caused by a pile-up in an adjacent grain. The modelling results showed good quantitative agreement with the analytical analysis, which was also extended to uniaxial tension loading to determine that a soft grain pile-up plane oriented 56.1° to the horizontal, an orientation easily achieved since there are three independent $\langle a \rangle$ prism slip planes spaced 60° apart, causes the greatest crack opening stress on the basal plane in the hard grain.

A polycrystalline model was created and subjected to normal fatigue loading and dwell fatigue loading. A so-called rogue grain combination, consisting of a hard grain adjacent to soft grains, was located in the centre of the model. Strong load shedding was observed during the stress-dwell period, which was predicted by the discrete dislocation plasticity model, particularly the internal stress fields due to discrete dislocation pile-ups operating at sub-grain length scales. While crystal plasticity methods have been demonstrated to successfully capture load shedding, the details of dislocation pile-ups and consequent back stress development are captured in addition by the discrete dislocation approach. A significant increase in the dislocation density was observed as a result of the dwell, due to continued source activation under sustained stress enhanced by the ability of dislocations to escape obstacles over time by a thermally activated process; on the contrary, the dislocation density at the end of normal fatigue loading was found to be much lower. This created much higher intensity pile ups in the soft grain under dwell loading, which generated high localised stresses in the hard grain that may be the cause of facet crack initiation. It is statistically probable that in a Ti alloy fan blade in an aircraft engine a worst case rogue grain combination will exist somewhere, with the hard grain c-axis roughly parallel to the primary loading direction and at least

one adjacent soft grain oriented such that one of its three independent $\langle a \rangle$ prism planes is approximately 60° degrees from the hard grain basal plane.

A bicrystal model was used to assess the extent that grain orientations, grain boundary morphology and loading direction combine to affect the grain boundary stresses in the hard grain. The scenario in which the grain boundary angle is parallel to an active slip system in the soft grain generated basal and pyramidal slip nucleation in the adjacent hard grain. The basal slip nucleation was initiated despite no resolved shear stress from the applied loading, but results from high stresses generated by strong pile ups in the soft grain.

The DDP calculations presented are two-dimensional and elastically isotropic, hence some features cannot be captured such as anisotropy, cross slip and dislocation dissociation etc. However, the main mechanism (and focus in this study) controlling the load shedding is argued to be the thermally activated dislocation escape from obstacles, and the 2D model presented which has point obstacles explicitly defined is believed to explain the dwell fatigue in α-titanium alloy reasonably well. Extensions of the model to 3D are believed to be possible and will be the focus of future work.

Acknowledgments

ZZ and FD acknowledge the financial support by the Engineering and Physical Sciences Research Council for funding through the HexMat programme grant EP/K034332/1 and the China Scholarship Council (CSC). FD gratefully acknowledges the Royal Academy of Engineering and Rolls-Royce for research chair support.

Appendix A. Derivation of uniaxial tension model I

The uniaxial tension model I, as illustrated in Fig. 5b, is directly compared with the original pure shear model by Stroh. The applied stress in the $x-y$ coordinate system is

$$\sigma = \begin{bmatrix} 0 & 0 \\ 0 & \sigma_0 \end{bmatrix} \tag{A-1}$$

In the $x' - y'$ system (45° counter clockwise rotation), the applied stress tensor becomes

$$\sigma' = \frac{\sigma_0}{2}\begin{bmatrix} 1 & 1 \\ 1 & 1 \end{bmatrix} \tag{A-2}$$

The resolved shear stress on the pile-up plane is $\tau_0 = \sigma_0/2$. The length of the pile up group, which consists of N positive edge dislocations, is given by Stroh (1954)

$$L_0^{t1} = \frac{GbN}{\pi(1-\nu)\tau_0} = \frac{GbN}{2\pi(1-\nu)\sigma_0} \tag{A-3}$$

and the stresses due to the (N−1) free dislocations are

$$\begin{aligned} &\frac{1}{2}\left(\sigma_{x'x'} + \sigma_{y'y'}\right)/\tau_0 = -3\sin\theta/2r + 2(n/r)^{\frac{1}{2}}\sin\frac{1}{2}\theta \\ &\frac{1}{2}\left(\sigma_{x'x'} - \sigma_{y'y'}\right)/\tau_0 = -3\sin\theta(1+\cos 2\theta)/2r + (n/r)^{\frac{1}{2}}\left(2\sin\frac{1}{2}\theta + \sin\theta\cos\frac{3}{2}\theta\right) \\ &\sigma_{x'y'}/\tau_0 = -1 - 3(\cos\theta - \sin\theta\sin 2\theta)/2r + (n/r)^{\frac{1}{2}}\left(2\cos\frac{1}{2}\theta - \sin\theta\sin\frac{3}{2}\theta\right) \end{aligned} \tag{A-4}$$

where the unit of length is chosen to be $Gb/4\pi(1-\nu)\tau_0$: the half equilibrium distance between two opposite dislocations under shear stress τ_0. The stresses due to the locked dislocation and the applied stress are given by

$$\begin{aligned} &\frac{1}{2}\left(\sigma_{x'x'} + \sigma_{y'y'}\right)/\tau_0 = 2\sin\theta/r + 1 \\ &\frac{1}{2}\left(\sigma_{x'x'} - \sigma_{y'y'}\right)/\tau_0 = 4\cos^2\theta\sin\theta/r \\ &\sigma_{x'y'}/\tau_0 = 2\cos\theta\cos 2\theta/r + 1 \end{aligned} \tag{A-5}$$

Combining Eqs. (A-4) and (A-5), the total stresses at the point $(r,0)$ are

$$\begin{aligned}
&\frac{1}{2}(\sigma_{x'x'}+\sigma_{y'y'})/\tau_0 = \sin\theta/2r + 2(n/r)^{\frac{1}{2}}\sin\frac{1}{2}\theta + 1\\
&\frac{1}{2}(\sigma_{x'x'}-\sigma_{y'y'})/\tau_0 = \sin\theta\cos^2\theta\Big/r + (n/r)^{\frac{1}{2}}\left(2\sin\frac{1}{2}\theta + \sin\theta\cos\frac{3}{2}\theta\right)\\
&\sigma_{x'y'}/\tau_0 = -\cos\theta\cos 2\theta/2r - (n/r)^{\frac{1}{2}}\left(2\cos\frac{1}{2}\theta - \sin\theta\sin\frac{3}{2}\theta\right)
\end{aligned} \tag{A-6}$$

Since r>1/N, we have $1/r < (N/r)^{\frac{1}{2}}$ and it is safe to neglect the terms contains 1/r. Eq. (A-6) becomes

$$\begin{aligned}
&\frac{1}{2}(\sigma_{x'x'}+\sigma_{y'y'})/\tau_0 = 2(n/r)^{\frac{1}{2}}\sin\frac{1}{2}\theta + 1\\
&\frac{1}{2}(\sigma_{x'x'}-\sigma_{y'y'})/\tau_0 = (n/r)^{\frac{1}{2}}\left(2\sin\frac{1}{2}\theta + \sin\theta\cos\frac{3}{2}\theta\right)\\
&\sigma_{x'y'}/\tau_0 = -(n/r)^{\frac{1}{2}}\left(2\cos\frac{1}{2}\theta - \sin\theta\sin\frac{3}{2}\theta\right)
\end{aligned} \tag{A-7}$$

The normal stress σ_n acting at the point $(r,0)$ on the positive x-axis is

$$\begin{aligned}
&\sigma_n = \frac{1}{2}(\sigma_{x'x'}+\sigma_{y'y'}) - \frac{1}{2}(\sigma_{x'x'}-\sigma_{y'y'})\cos 2\theta - \sigma_{x'y'}\sin 2\theta\\
&\frac{\sigma_n}{\sigma_0} = \frac{3}{4}\left(\frac{L_0^{t1}}{r}\right)^{\frac{1}{2}}\sin\theta\cos\frac{1}{2}\theta + \frac{1}{2}
\end{aligned} \tag{A-8}$$

Appendix B. Derivation of uniaxial tension model II

The uniaxial tension model II, as illustrated in Fig. 5c, is developed from the original pure shear model. The applied stress in the x–y coordinate system is

$$\sigma = \begin{bmatrix} 0 & 0 \\ 0 & \sigma_0 \end{bmatrix} \tag{B-1}$$

In the counter clock wise rotated $x' - y'$ system, the applied stress tensor becomes

$$\sigma' = \sigma_0\begin{bmatrix} \sin^2\theta & \sin\theta\cos\theta \\ \sin\theta\cos\theta & \cos^2\theta \end{bmatrix} \tag{B-2}$$

where θ is the rotation angle, which is equal to the angle between the slip plane and the x-axis The resolved shear stress on the pile-up plane is $\tau_0 = \sigma_0 sin\theta cos\theta$. The length of the pile up group, which consists of N positive edge dislocations, is given by Stroh (1954)

$$L_0^{t2} = \frac{GbN}{\pi(1-\nu)\tau_0} = \frac{GbN}{\pi(1-\nu)\sigma_0\sin\theta\cos\theta} \tag{B-3}$$

and the stresses due to the $(N-1)$ free dislocations are

$$\begin{aligned}
&\frac{1}{2}(\sigma_{x'x'}+\sigma_{y'y'})/\tau_0 = -3\sin\theta/2r + 2(n/r)^{\frac{1}{2}}\sin\frac{1}{2}\theta\\
&\frac{1}{2}(\sigma_{x'x'}-\sigma_{y'y'})/\tau_0 = -3\sin\theta(1+\cos 2\theta)/2r + (n/r)^{\frac{1}{2}}\left(2\sin\frac{1}{2}\theta + \sin\theta\cos\frac{3}{2}\theta\right)\\
&\sigma_{x'y'}/\tau_0 = -1 - 3(\cos\theta - \sin\theta\sin 2\theta)/2r + (n/r)^{\frac{1}{2}}\left(2\cos\frac{1}{2}\theta - \sin\theta\sin\frac{3}{2}\theta\right)
\end{aligned} \tag{B-4}$$

where the unit of length is chosen to be $Gb/4\pi(1-\nu)\tau_0$: the half equilibrium distance between two opposite dislocations under shear stress τ_0. The stresses due to the locked dislocation and the applied stress are given by

$$\begin{aligned}
&\frac{1}{2}\left(\sigma_{x'x'}+\sigma_{y'y'}\right)/\tau_0 = 2\sin\theta/r + 1/\sin 2\theta \\
&\frac{1}{2}\left(\sigma_{x'x'}-\sigma_{y'y'}\right)/\tau_0 = 4\cos^2\theta\sin\theta\Big/r - \cos 2\theta/\sin 2\theta \\
&\sigma_{x'y'}/\tau_0 = 2\cos\theta\cos 2\theta/r + 1
\end{aligned} \tag{B-5}$$

Combining Eqs. (B-4) and (B-5), the total stresses at the point (r,0) are

$$\begin{aligned}
&\frac{1}{2}\left(\sigma_{x'x'}+\sigma_{y'y'}\right)/\tau_0 = \sin\theta/2r + 2(n/r)^{\frac{1}{2}}\sin\frac{1}{2}\theta + 1/\sin 2\theta \\
&\frac{1}{2}\left(\sigma_{x'x'}-\sigma_{y'y'}\right)/\tau_0 = \sin\theta\cos^2\theta\Big/r + (n/r)^{\frac{1}{2}}\left(2\sin\frac{1}{2}\theta + \sin\theta\cos\frac{3}{2}\theta\right) - \cos 2\theta/\sin 2\theta \\
&\sigma_{x'y'}/\tau_0 = -\cos\theta\cos 2\theta/2r - (n/r)^{\frac{1}{2}}\left(2\cos\frac{1}{2}\theta - \sin\theta\sin\frac{3}{2}\theta\right)
\end{aligned} \tag{B-6}$$

Since r>1/N, we have $1/r < (N/r)^{\frac{1}{2}}$ and it is safe to neglect the terms contains 1/r. Eq. (B-6) becomes

$$\begin{aligned}
&\frac{1}{2}\left(\sigma_{x'x'}+\sigma_{y'y'}\right)/\tau_0 = 2(n/r)^{\frac{1}{2}}\sin\frac{1}{2}\theta + 1/\sin 2\theta \\
&\frac{1}{2}\left(\sigma_{x'x'}-\sigma_{y'y'}\right)/\tau_0 = (n/r)^{\frac{1}{2}}\left(2\sin\frac{1}{2}\theta + \sin\theta\cos\frac{3}{2}\theta\right) - \cos 2\theta/\sin 2\theta \\
&\sigma_{x'y'}/\tau_0 = -(n/r)^{\frac{1}{2}}\left(2\cos\frac{1}{2}\theta - \sin\theta\sin\frac{3}{2}\theta\right)
\end{aligned} \tag{B-7}$$

The normal stress σ_n acting at the point $(r,0)$ on the positive x-axis is

$$\begin{aligned}
&\sigma_n = \frac{1}{2}\left(\sigma_{x'x'}+\sigma_{y'y'}\right) - \frac{1}{2}\left(\sigma_{x'x'}-\sigma_{y'y'}\right)\cos 2\theta - \sigma_{x'y'}\sin 2\theta \\
&\frac{\sigma_n}{\sigma_0} = \frac{3}{2}\left(\frac{L_0^{t2}}{r}\right)^{\frac{1}{2}}\sin^2\theta\cos\theta\cos\frac{1}{2}\theta + \frac{1}{2}\sin^2 2\theta
\end{aligned} \tag{B-8}$$

References

Adenstedt, H., 1949. Creep of titanium at room temperature. Metal. Prog. 56.
Agnihotri, P.K., Van der Giessen, E., 2015. On the rate sensitivity in discrete dislocation plasticity. Mech. Mater. 90, 37–46.
Bache, M., Dunne, F., Madrigal, C., 2010. Experimental and crystal plasticity studies of deformation and crack nucleation in a titanium alloy. J. Strain Anal. Eng. Des. 45, 391–399.
Bache, M.R., 1999. Processing titanium alloys for optimum fatigue performance. Int. J. Fatigue 21 (Suppl. 1), S105–S111.
Bache, M.R., 2003. A review of dwell sensitive fatigue in titanium alloys: the role of microstructure, texture and operating conditions. Int. J. Fatigue 25, 1079–1087.
Bache, M.R., Cope, M., Davies, H.M., Evans, W.J., Harrison, G., 1997. Dwell sensitive fatigue in a near alpha titanium alloy at ambient temperature. Int. J. Fatigue 19, 83–88.
Balint, D.S., Deshpande, V.S., Needleman, A., Giessen, E.V.d., 2006. Size effects in uniaxial deformation of single and polycrystals: a discrete dislocation plasticity analysis. Model. Simul. Mater. Sci. Eng. 14, 409.
Balint, D.S., Deshpande, V.S., Needleman, A., Van der Giessen, E., 2008. Discrete dislocation plasticity analysis of the grain size dependence of the flow strength of polycrystals. Int. J. Plasticity 24, 2149–2172.
Bridier, F., McDowell, D.L., Villechaise, P., Mendez, J., 2009. Crystal plasticity modeling of slip activity in Ti–6Al–4V under high cycle fatigue loading. Int. J. Plasticity 25, 1066–1082.
Conrad, H., 1967. Thermally activated deformation of α titanium below 0.4 TM. Can. J. Phys. 45, 581–590.
Cottrell, A.H., Dexter, D., 1954. Dislocations and plastic flow in crystals. Am. J. Phys. 22, 242–243.
Dunne, F.P.E., Rugg, D., 2008. On the mechanisms of fatigue facet nucleation in titanium alloys. Fatigue & Fract. Eng. Mater. Struct. 31, 949–958.
Dunne, F.P.E., Rugg, D., Walker, A., 2007a. Lengthscale-dependent, elastically anisotropic, physically-based hcp crystal plasticity: application to cold-dwell fatigue in Ti alloys. Int. J. Plasticity 23, 1061–1083.
Dunne, F.P.E., Walker, A., Rugg, D., 2007b. A systematic study of hcp crystal orientation and morphology effects in polycrystal deformation and fatigue. Proc. R. Soc. Lond. A Math. Phys. Eng. Sci. 463, 1467–1489.
Evans, W.J., Bache, M.R., 1994. Dwell-sensitive fatigue under biaxial loads in the near-alpha titanium alloy IMI685. Int. J. Fatigue 16, 443–452.
Ghosh, S., Anahid, M., 2013. Homogenized constitutive and fatigue nucleation models from crystal plasticity FE simulations of Ti alloys, Part 1: macroscopic anisotropic yield function. Int. J. Plasticity 47, 182–201.
Gibbs, G.B., 1969. Thermodynamic analysis of dislocation glide controlled by dispersed local obstacles. Mater. Sci. Eng. 4, 313–328.
Hasija, V., Ghosh, S., Mills, M.J., Joseph, D.S., 2003. Deformation and creep modeling in polycrystalline Ti–6Al alloys. Acta Mater. 51, 4533–4549.
Littlewood, P.D., Britton, T.B., Wilkinson, A.J., 2011. Geometrically necessary dislocation density distributions in Ti–6Al–4V deformed in tension. Acta Mater. 59, 6489–6500.

Przybyla, C.P., McDowell, D.L., 2011. Simulated microstructure-sensitive extreme value probabilities for high cycle fatigue of duplex Ti–6Al–4V. Int. J. Plasticity 27, 1871–1895.
Sinha, V., Mills, M.J., Williams, J.C., Spowart, J.E., 2006. Observations on the faceted initiation site in the dwell-fatigue tested ti-6242 alloy: crystallographic orientation and size effects. Metall Mat Trans A 37, 1507–1518.
Stroh, A.N., 1954. The formation of cracks as a result of plastic flow. Proc. R. Soc. Lond. A Math. Phys. Eng. Sci. 223, 404–414.
Tarleton, E., Balint, D.S., Gong, J., Wilkinson, A.J., 2015. A discrete dislocation plasticity study of the micro-cantilever size effect. Acta Mater. 88, 271–282.
Taylor, G.I., 1934. The mechanism of plastic deformation of crystals. Part I. Theoretical. Proc. R. Soc. Lond. Ser. A, Contain. Pap. Math. Phys. Character 145, 362–387.
Van der Giessen, E., Needleman, A., 1995. Discrete dislocation plasticity: a simple planar model. Model. Simul. Mater. Sci. Eng. 3, 689.
Venkataramani, G., Kirane, K., Ghosh, S., 2008. Microstructural parameters affecting creep induced load shedding in Ti-6242 by a size dependent crystal plasticity FE model. Int. J. Plasticity 24, 428–454.
Venkatramani, G., Ghosh, S., Mills, M., 2007. A size-dependent crystal plasticity finite-element model for creep and load shedding in polycrystalline titanium alloys. Acta Mater. 55, 3971–3986.
Whittaker, M., 2011. Titanium in the Gas Turbine Engine. INTECH Open Access Publisher.
Zhang, P., Balint, D., Lin, J., 2011. Controlled Poisson Voronoi tessellation for virtual grain structure generation: a statistical evaluation. Philos. Mag. 91, 4555–4573.
Zhang, Z., Cuddihy, M.A., Dunne, F.P.E., 2015. On rate-dependent polycrystal deformation: the temperature sensitivity of cold dwell fatigue. Proc. R. Soc. Lond. A Math. Phys. Eng. Sci. 471.
Zheng, Z., Balint, D.S., Dunne, F.P.E., 2016. Rate sensitivity in discrete dislocation plasticity in hexagonal close-packed crystals. Acta Mater. 107, 17–26.